



OPEN

Laser Modified ZnO/CdS_{Se} Core-Shell Nanowire Arrays for Micro-Steganography and Improved Photoconduction

SUBJECT AREAS:
NANOSCALE MATERIALS
NANOSCALE DEVICES
NANOWIRES
OPTICAL TECHNIQUES

Received
10 June 2014

Accepted
22 August 2014

Published
12 September 2014

Correspondence and requests for materials should be addressed to H.W.L. (liuhw@imre.a-star.edu.sg) or C.H.S. (physowch@nus.edu.sg)

Junpeng Lu¹, Hongwei Liu², Minrui Zheng¹, Hongji Zhang¹, Sharon Xiaodai Lim¹, Eng Soon Tok¹ & Chong Haur Sow¹

¹Department of Physics, 2 Science Drive 3, National University of Singapore, 117542, Singapore, ²Institute of Materials Research and Engineering, A*STAR (Agency for Science, Technology and Research), 3 Research Link, 117602, Singapore.

Arrays of ZnO/CdS_{Se} core/shell nanowires with shells of tunable band gaps represent a class of interesting hybrid nanomaterials with unique optical and photoelectrical properties due to their type II heterojunctions and chemical compositions. In this work, we demonstrate that direct focused laser beam irradiation is able to achieve localized modification of the hybrid structure and chemical composition of the nanowire arrays. As a result, the photoresponsivity of the laser modified hybrid is improved by a factor of ~ 3 . A 3D photodetector with improved performance is demonstrated using laser modified nanowire arrays overlaid with monolayer graphene as the top electrode. Finally, by controlling the power of the scanning focused laser beam, micropatterns with different fluorescence emissions are created on a substrate covered with nanowire arrays. Such a pattern is not apparent when imaged under normal optical microscopy but the pattern becomes readily revealed under fluorescence microscopy *i.e.* a form of Micro-Steganography is achieved.

Band gap engineering is an attractive strategy for the control of physical properties of semiconductors in photoelectronics^{1–5}. Band gap engineering of multinary alloyed nanostructures has been achieved by adjusting their relative composition as these alloys show a strong dependence of electronic energy on the effective exciton mass^{6–9}. In addition, another approach to achieve band gap engineering is the controlled synthesis of hetero/hybrid nanostructures. Among these structures, the band gap in type II core/shell heterostructures forms a stepwise energy alignment at the interfaces where both the conduction and the valence bands of the shell are either higher or lower in energy than those in the core. Majority and minority carriers would preferably transfer across the junction in opposite directions to form an excitonic charge separation state^{10,11}. Emission or absorption of photons by recombination or separation of holes confined in core/shell and electrons confined in shell/core occurs across the junction would present a lower energy configuration than the band gaps of either the core component or the shell component¹. This represents a new handle to band gap engineering. Therefore, type II core/shell heterostructures with multinary alloyed constituents would enable a multidimensional control of band gap engineering to fabricate samples with highly tunable physical properties and extended application potentials^{12–14}. However, while the electrical properties of these type II core/shell heterostructures can be distinctly improved, their optical property is greatly affected due to the ease with which electron and hole separate at the interface. This will limit the implementation of type II core/shell nanostructures in photonics circuits and optoelectronic devices. Therefore, a simple, flexible, efficient, and low cost post-synthesis technique is highly desirable to modify and improve the optical property of type II core/shell nanostructures. For this purpose, we developed a facile and effective focused laser pruning method which can controllably modify the chemical composition of type II core/shell nanostructures. Focused laser beam is a versatile technique for post-synthesis treatment of nanomaterials. Many complex phenomena such as photo-oxidation, photochemical reaction, photodestruction, photophysical modification, etc. could be triggered with this process. The extent of chemical modification becomes richer if the environment during the implementation of focused laser irradiation is further regulated. For example, we can easily assemble or decorate single crystalline thin film or metal nanoparticles onto the nanostructures using focused laser beam modification in corresponding chemical solutions^{15,16}. Considering



the fast rastering speed and high energy intensity of lasers, laser modification is a rapid and quenching process as compared with other slower process.

To the best of our knowledge, this is a first report on the modification of hybrid ZnO/CdSSe core-shell nanowire arrays utilizing a scanning focused laser beam. By controlling the power of the scanning focused laser beam, micropatterns with different fluorescence emissions are created on a substrate covered with these hybrid nanowire arrays. If the pattern is created using low laser power, such a pattern is not apparent when imaged under normal optical microscopy but the pattern becomes readily revealed under fluorescence microscopy *i.e.* we have achieved a form of Micro-Steganography. In addition to the modification of the optical properties of the hybrid nanowires, the focused laser modification could also be simultaneously utilized to modify the electrical properties of these hybrid nanowires. In doing so, we strive to achieve a good balance in the control of the optical and electrical properties of the type II core/shell nanostructures en route to functional optoelectronic devices. Based on this, a high performance 3D photodetector is fabricated and demonstrated using laser pruned ZnO/CdSSe nanowire arrays with monolayer graphene as transparent top electrode. The construction of micropatterns with functionality/fluorescence control within the nanowire arrays would provide greater building blocks for optoelectronic applications.

Results

The nanowire arrays studied in this work consist of vertically aligned hybrid ZnO/CdSSe core/shell nanowires grown epitaxially on quartz substrates with pre-deposited 200 nm ZnO film using a sequential 2-step vapor-solid growth^{12,13} (see Methods). Notably, vertically aligned nanowires with high uniformity covering an area of more than 1 cm² are fabricated¹⁷. The composition and thickness of the shells is accurately controlled¹⁸. Figure 1a shows SEM images of the

nanowire arrays before and after CdSSe shell deposition. These images clearly show the quasi-vertical alignment of the nanowires. Other crystalline structural characterizations are demonstrated by the TEM and HRTEM images. The stoichiometric uniformity is determined by the EDX mapping and line scans along an individual nanowire. Details of these characterizations are shown in Supplementary Section (S1).

Direct modification of the hybrid core-shell nanowires is carried out through a focused laser beam setup. Figure 1b shows the schematic diagram of the experimental setup. In this setup, a diode laser is employed as the source of the laser beam. In separate experiments, we have made use of two different types of diode laser in this work. Namely, one of the laser sources emits laser beam with a wavelength of 660 nm at a maximum power of 70 mW at source while the other laser source emits laser beam with a wavelength of 532 nm at a maximum laser power of 200 mW at source. The emitted laser beam is guided into an optical microscope through the reflection of two mirrors. Inside the microscope, the laser beam is directed toward an objective lens by a beam splitter. We have different types of objective lenses in this setup and we can select one with a magnification of 50× or 100× for our experiments. After passing through the objective lens, the laser beam is tightly focused onto the surface of a sample. The sample is mounted on a motorized stage which is flexibly moveable in X-Y direction. A CCD camera is used to monitor the process of laser modification and examine the quality of the pattern. When the laser beam is focused upon the nanowire arrays, the laser energy absorbed by the CdSSe shell is rapidly converted to local heat. The intense heat raises the temperature of irradiated nanowire tops and causes localized modification of the core/shell structure. This modification technique is akin to lawn pruning and thus we denote it as the laser pruning method. By controlling the stage movement in a programmable manner, micropatterns are constructed on the nanowire arrays. Figure 1c shows a SEM image of a micro pattern fabricated

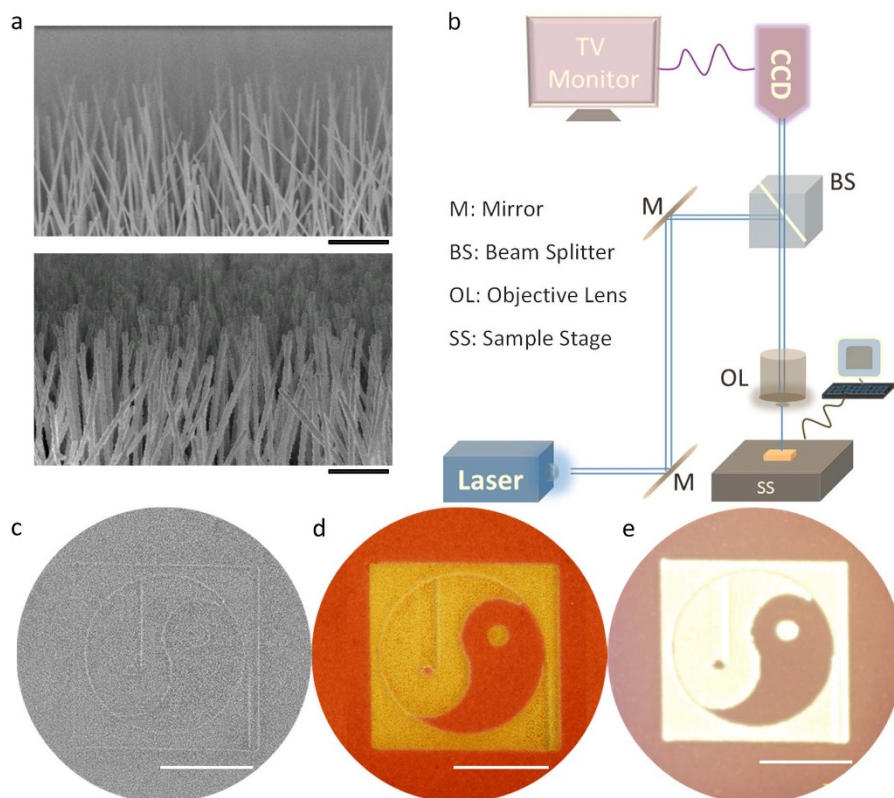


Figure 1 | (a) SEM images of as-grown ZnO nanowire arrays (upper image) and ZnO/CdSSe core/shell nanowire arrays (lower image). Scale bars are equivalent to 1 μm . (b) Schematic of focused laser beam set-up. (c) – (e) SEM, bright field optical, and FM images respectively of a micro-pattern created. Scale bars are equivalent to 200 μm .



using this method and Figures 1d and e show the same pattern observed using a bright field microscope and fluorescence microscope, respectively. Note that in this case, the laser source that emits laser beam with a wavelength of 660 nm at a power of 50 mW is utilized. The SEM image does not reveal a striking contrast from the created microstructure. This is because the length of the core/shell nanowires is not significantly affected. However, the reflectivity of the pruned regions becomes different from the pristine regions. As a result, the bright field optical image provides a clearer contrast. The bright orange background is reminiscent of the optical properties of the pristine nanowires. Prominently, the laser modified region exhibits a different reflective color which is bright yellow. Therefore, the micropattern becomes more visible. Perhaps the most significant change in the nanowire array is displayed by the image captured by the fluorescence microscope. The weak reddish-orange background originates from the pristine core/shell nanowires. CdSSe nanostructures possess high yield luminescence. Nevertheless, the formation of type II core/shell architecture impedes the irradiative carrier recombination. Therefore, only weak fluorescence emission is achieved upon UV excitation. Remarkably, laser treated nanowire array exhibits a different fluorescence behavior. The laser pruned region emits a dazzling quasi-white color and the difference in this color from the pristine nanowire array results in the best contrast among the three types of images. Clearly, the laser modified nanowires have been innovated into another type of material which shows different fluorescence property. This is a surprising result considering the destructive attribute of a high energy focused laser beam.

Quantitative investigations on the fluorescence behavior are carried out by the micro-photoluminescence spectroscopy. Figure 2a shows the photoluminescence spectra for pristine and laser pruned regions, respectively. The laser pruning is carried out with the diode laser with center wavelength at 660 nm and the laser power is maintained at 50 mW. Evidently, the pristine region shows a narrower peak with the peak located at 581.7 ± 0.1 nm. This corresponds to the reddish-orange color from the fluorescence microscope observation. As evident from Figure 2a, after patterning with focused laser beam, the intensity of photoluminescence peak significantly increases and the base of the peak has become broadened. As a comparison, the PL spectra of pure ZnO and CdSSe were shown in Supplementary Section 2. The significant change of the optical property indicates that the formation of a different material upon laser

pruning. As revealed by the SEM images (Figure 2b), the laser pruning creates micropatterns consisting of quasi-1D nanomaterial arrays with morphology that is very different from the pristine nanowires. The low magnification and high magnification TEM images of the laser modified nanowires are shown in Supplementary Section S3. The new morphology of the hybrid takes the form of nanoparticle clusters gathered on the top of the nanowires. The formation of the nanoparticle cluster is akin to an explosion of the tiptop of the nanowire, whilst the rest of the nanowires remain unaffected. The formation of the nanoparticle represents a different type of material with different stoichiometry. As revealed by the EDX spectra carried on the pristine (Figure 2c) and laser treated (Figure 2d) region, laser modification increases the atomic ratio of Oxygen-“O” from 19.97% to 34.17%. Conversely, laser modification decreases the Sulphur-“S” element from 22.77% to 17.25%. With the control in altering the stoichiometry of the sample, this laser pruning can construct micropatterns with uniform and controlled element distribution. Figures 2e and f show the EDX elemental mapping of oxygen-“O” in a micro-rectangle and sulphur-“S” in a micro-flower, respectively. Clearly the laser pruned region shows an enriched signal in oxygen “O” and reduction in the sulphur “S”. The EDX elemental mappings (Fig. 2e and f) also demonstrate the uniform distribution of the elements inside the laser created patterns. In addition to the stoichiometry variation, the formation of the nanoparticle cluster is indicative of the destruction of the core/shell structure on the top of the nanowires. This “exposed” structure facilitates the significant increase in the photoluminescence intensity because of the co-existence of the emission color from newly formed nanoparticles. The quantum confinement effect of the nanoparticles could also contribute to the broadening of the emission spectrum. As shown in Supplementary Section S3c, the HRTEM indicates that the nanoparticles are crystalline with the size smaller than 10 nm. It is possibly formatted by alloying among ZnO and CdSSe to facilitate the formation of quaternary compounds. Furthermore additional defects are introduced into the ZnO and CdSSe due to the laser irradiation and these defects can contribute their corresponding defect peaks in photoluminescence study. All these factors contribute to the broadening of the photoluminescence spectrum and consequently facilitate the quasi-white light emission.

As observed, the nanoparticle cluster is only constructed on the tip of the nanowires. This is caused by the heat energy accumulation at

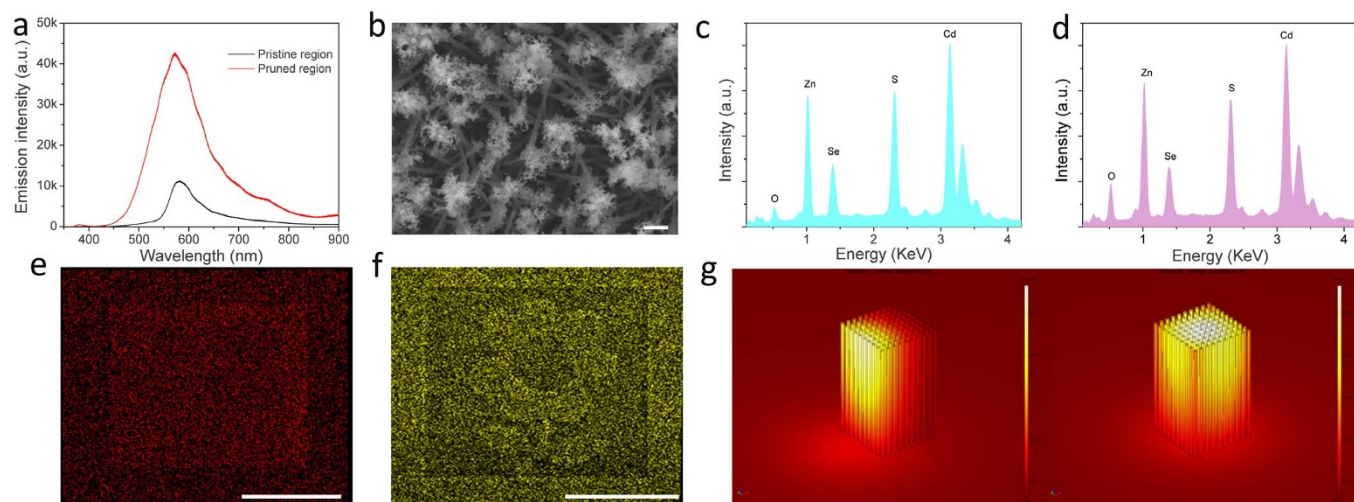


Figure 2 | (a) PL spectra for pristine region (black curve) and laser pruned region (red curve) using a diode laser that emits laser beam of wavelength of 660 nm at 50 mW. (b) SEM image of the nanowire array after laser pruning. Scale bar is 2 μ m. EDX spectra of (c) pristine and (d) laser pruned region. EDX mapping of (e) Oxygen-“O” in a micro-rectangle and (f) Sulphur-“S” in a micro-flower. Scale bar is 100 μ m in (e) and 200 μ m in (f). (g) FEM simulation result of temperature distribution along the nanowire array. Laser was scanning from left to right. Evidently, most of the thermal energy was restricted at the top of nanowires resulting in the highest temperature at that region.



the top of the nanowires. When the laser beam is focused upon the top of the nanowires, the absorbed laser energy is rapidly converted to local heat. Due to the ultralow thermal conductivity of the CdSSe alloys (as measured in Supplementary Section S4, the calculated thermal conductivity coefficient $\kappa < 1 \frac{W}{mK}$), the heat energy cannot be transmitted efficiently to the rest of the nanowires and the substrate. Therefore, most of the heat energy is retained at the tip of the nanowires. The gathering of the high temperature at such small location causes the nanowire tips to “explode” to nanoparticle clusters. We carry out additional investigation on the laser induced heat distribution in these nanowires array by the finite element method (FEM) simulation. A model with 100 core/shell nanowires is built. The laser beam is rastered over the surface of the nanowire array at a speed of 100 $\mu\text{m/s}$. Figure 2g shows the 3-dimensional temperature distribution in the nanowires array after laser scanning of 0.01 s and 0.05 s, respectively. Evidently, most of the heating energy is found localized at the top part of the nanowires. The dynamic process of the temperature distribution is shown in the Supplementary Section (.gif file).

Discussion

Systematic studies on the detailed change in the optical property caused by the laser modification are carried out. Low temperature and time-resolved photoluminescence spectra are measured with the excitation of a pulsed diode laser operating at 405 nm. In order to gain greater insight into the effects of laser pruning on the carrier localization, the photoluminescence spectra of pristine and pruned regions at a series of temperatures from 5 K to 300 K are carried out

and shown in Supplementary Section S5. As the temperature decreases, the main peak of both regions increases remarkably in intensity, whilst the peak position gradually blue shifts with decreasing temperature. This blue-shift with temperature indicates the expansion of band gap due to the suppression of both exciton-phonon interaction and thermal expansion^{19–21}. However, in contrast to the room temperature photoluminescence, the spectrum of pristine region exhibits much higher intensity than that of laser modified region at 5 K (Figure 3a). This is because low temperature restrains the thermal energy loss and carriers transport, which will in turn suppress the separation of electron-hole pair at the type II core/shell interface. Therefore, excitons are restricted inside the CdSSe shell and thus irradiative recombination is enhanced. By applying peak separation fitting on the spectrum (Supplementary Section S5), all the peaks can be attributed to the recombination of free exciton A (FXA), free exciton B (FXB), spatially localized donor-acceptor pairs (DAP) and a series of longitudinal photon (LO) replicas of DAP in CdSSe^{22,23}. Relatively, due to the small particle size and high density of defects of the laser modified region, the temperature effects on the carrier localization and decay are less distinct than that shown by pristine region. Further evidence can be revealed from the time-resolved photoluminescence measurements which will provide details of the exciton dynamics. Figure 3b shows the photoluminescence decay traces of pristine region, laser pruned region and pure CdSSe nanostructures (CdSSe nanowires without ZnO core) measured at 300 K. Evidently, both the laser pruned region and the pristine region exhibit much faster decay than pure CdSSe nanostructure. By applying exponential function fitting on the experimental measurements, the laser pruned sample is found to exhibit

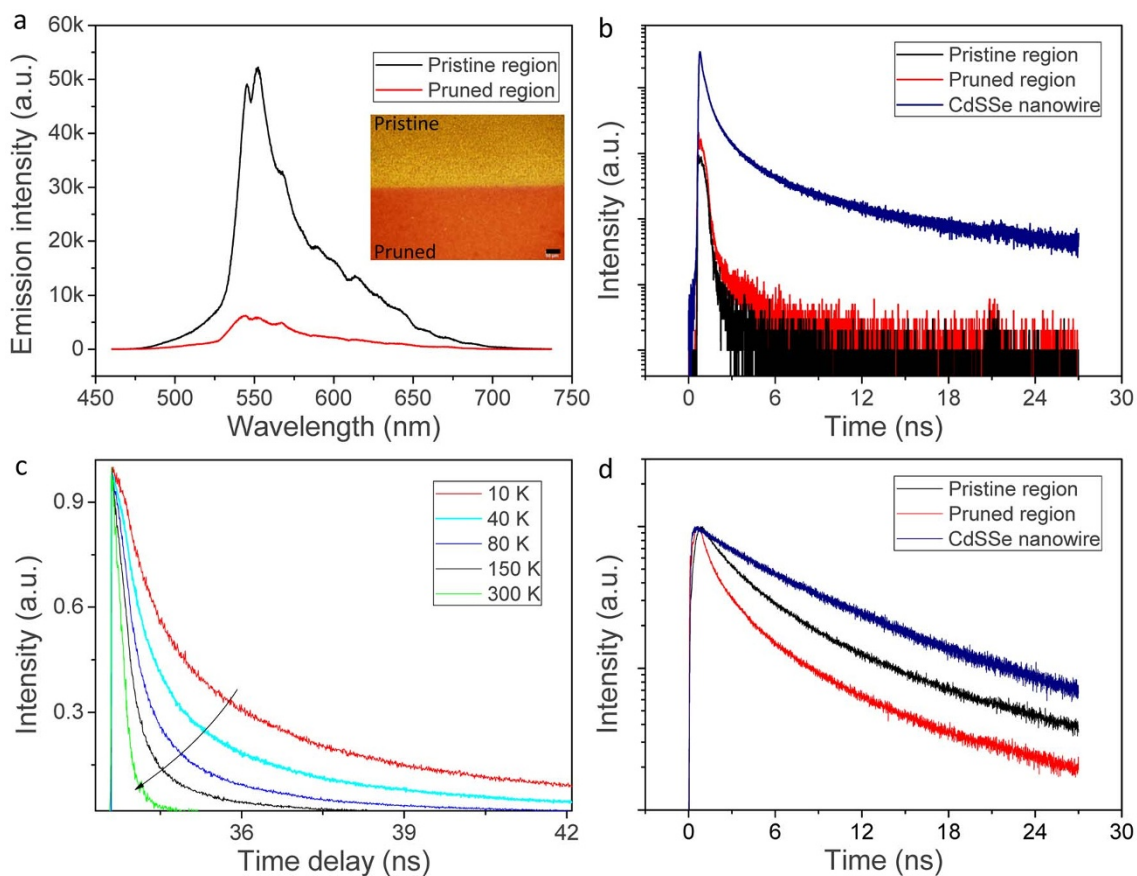


Figure 3 | (a) PL spectra of pristine (black curve) and laser pruned (red curve) regions measured at 5 K. Insert shows the bright field image of the pristine and pruned regions (created by 660 nm diode laser at 50 mW) used for low-temperature and time-resolved PL measurements. Scale bar is 50 μm . (b) PL decay traces of pristine region, laser pruned region and pure CdSSe nanostructures at 300 K. (c) Temperature depend PL decay traces of laser pruned sample. (d) PL decay traces of pristine region, laser pruned region and pure CdSSe nanostructures at 5 K.



the shortest photoluminescence lifetime, as listed in Supplementary Section S5. Inside the laser pruned nanostructures, a number of processes such as defect or boundary related trapping, thermal energy induced carrier delocalization, exciton dissociation, and non-radiative recombination can affect the carrier recombination. So the presence of many recombination paths results in the fast decay of the photoluminescence in laser pruned nanostructures. The ultrashort photoluminescence lifetime opens the possibility for implementation of laser modified nanostructures in ultrafast switching devices. In our previous study, the characteristic timescale for photoluminescence decay of the pure CdSSe nanostructures did not show monotonic variation with temperature. In contrast to previous result, the photoluminescence lifetime of the laser pruned nanostructure (Figure 3c) increases monotonically with decreasing temperature. This result is in contrast to the behavior observed in most conventional semiconductors whose photoluminescence lifetime decreases with decreasing temperature^{24,25}. The increase of the lifetime can be attributed to the decrease in the number of additional recombination paths for the excitons as the temperature decreases. As a result, the photoluminescence lifetime of these two samples are increased when compared with the pure CdSSe nanostructure at 5 K, as shown in Figure 3d. Due to the large number of the intrinsic recombination paths, the laser pruned complex nanostructure still exhibit the shortest lifetime among these three samples.

Due to the different absorption responses to different wavelength lasers, the nanowire arrays can also be pruned by focused green laser beam ($\lambda = 532$ nm). Remarkably, the pruned nanowires show significantly different morphology as compared with those modified by red laser ($\lambda = 660$ nm) (Figure 2a and b). As shown in the SEM image (Figure 4a), matchstick-like nanostructures are created by the green laser pruning. Beside the morphology difference, photoluminescence emission is also widened and enhanced (Figure 4b). However, the increase in the intensity of the photoluminescence is lower than sample modified by laser with a wavelength of 660 nm. By careful control of the laser powers, different fluorescence emission can be observed. Figures 4c and d show optical and FM images for four micro-boxes created with the focused laser beam using different laser powers (3 mW, 5 mW, 16 mW, and 18 mW for I, II, III, and IV, respectively). Evidently, different emission colors are observed under blue light excitation. Systematic studies on the dependence of such laser modification on the power of the laser beam are carried out. A set of patterned micro-squares are created using laser beam with different laser powers. The corresponding characterizations of FM images, optical microscope images, SEM images and PL spectra are carried out and shown in Supplementary Section S6. Once we have established control over the optical properties of the as-grown nanowire arrays and the laser pruned arrays, we can engineer functional components with interesting applications. As an example, we can construct hidden image (micro-steganography) onto a substrate with aligned nanowire arrays. Figures 4e and f show an example of such a hidden image. We create a micro-square on the nanowire array using a low laser power (~ 2 mW). Under bright field optical microscopy, nothing can be observed as shown in Figure 4ei. The laser power used is so low that the laser modified nanowires do not show any apparent difference from the as-grown nanowires so the micro-square is not distinguishable. However, where the same feature is imaged under fluorescence microscopy as shown in Figure 4eii (UV light excitation) and eiii (blue light excitation), the hidden micro-square is revealed readily. More complex micro-steganography is demonstrated in Figure 4f. Firstly, we use a high laser power of 18 mW to create the boundary of a box so that the box is visible under bright field optical microscopy imaging as illustrated in Figure 4fi. Then we use a lower laser power (~ 2 mW) to create a micro-dragon within the box. The clear micro-encryption effect is demonstrated under fluorescence microscopy. The colored micro-dragon is obviously displayed under both UV (Figure 4fii) and blue light

(Figure 4fiii) excitation. Thus this achieves the goal of hidden message creation and demonstrates the protocol for effective read-out.

Besides the modification in the optical properties, the laser pruned nanostructure system can be further functionalized to increase its potential applications. In our previous study, CdSSe nanostructure has been demonstrated to be a potential photoelectronic material with high photoconductivity^{26,27}. Laser pruned CdSSe has been shown to exhibit superior light trapping ability in comparison to the pristine counterpart²⁸. In recent research progress, graphene has been demonstrated to be a good transparent electrode due to its high degree of transparency^{29–31}. We seek to combine the unique characteristics of the different components and create a hybrid system that shows potential in optoelectronic applications. A 3D device architecture is designed based on the assembly of monolayer graphene onto laser pruned (or pristine) ZnO/CdSSe nanowire arrays en route to unique functional 3D microstructures. To assemble the designed device architecture, the steps illustrated in Figure 5a are carried out. The graphene electrode is transferred from a CVD grown graphene on copper substrate through a standard transfer process as described previously^{32,33}. Figure 5b shows the SEM images of the assembled hybrid structures consist of graphene on a typical nanowire array and laser pruned nanowire array, respectively. Note that the red laser beam is utilized in this case. Evidently, the monolayer graphene sheet is observed to overlay across individual nanowires on top of the pristine hybrid nanowire array and across the densified nanostructures on laser pruned array. A top-down, two probe technique is implemented for electrical transport measurements of the 3D structure. Figure 5c shows the typical I-V characteristics of the 3D devices based on pristine nanowire array (D1) and laser pruned nanowire array (D2). Clearly, the pristine nanowire arrays are poor conductors. We measure only a small current of 1.4×10^{-10} A through D1 at an applied bias of 4 V. However, D2 shows a significant increase in conductivity. We measure a current of 2.3×10^{-9} A at an applied voltage of 4 V. Such an improvement can be attributed to the obvious increase of the contact area (see from the SEM images Figure 5bii and iv) between the graphene electrode and the nanowire arrays. As shown by the SEM images, the expanded tip of the laser pruned nanowires gives rise to an increase in surface area at the top of the nanowire array and this helps to ensure better contact with the graphene electrode. Whilst, the focused laser induced compositional modification to the nanowire tops might possibly alter the electrical transport of the device. Besides a clear difference in conductivity, D1 and D2 also exhibited marked difference in photo-detection performance. Figure 5d shows the photoresponse characteristic of both photodetectors under applied bias at 4 V with broad beam laser illumination (4 mW/cm^2 , $\lambda = 405$ nm). Both devices exhibit increased output current under illumination, indicating their obvious photoresponse to 405 nm laser light. However, D2 shows a higher photoresponsivity which can be calculated by³⁴

$$R_{res} = \frac{I_{ph}}{P_{opt}} = \frac{(I_{illus} - I_{dark})S^{-1}}{P_{inc}} \quad (1)$$

where P_{opt} is light power, I_{illus} and I_{dark} are output current under illumination and in dark, respectively, S is effective area of nanowire device, and P_{inc} is power density of the incident light. It is very attractive that the responsivity of D2 can reach as high as 144.3 mA/W under 4 mW/cm^2 illumination, whilst the responsivity of D1 is measure to be only 50 mA/W under same illumination condition. The higher responsivity supports the potential applications of D2 in optoelectronic devices such as retro-sensors, optoisolators and photoamplifiers^{34,35}. Nevertheless, despite the lower responsivity, D1 also possesses its unique advantage. Namely, the photocurrent of D1 increases 146 times when compared to that measured at dark condition. This represents a high on/off ratio ($(I_{pho} - I_{dark})/I_{dark}$) in the range of 102 under 4 mW/cm^2 illumination. As comparison, the on/off ratio of D2 is measured to be less than

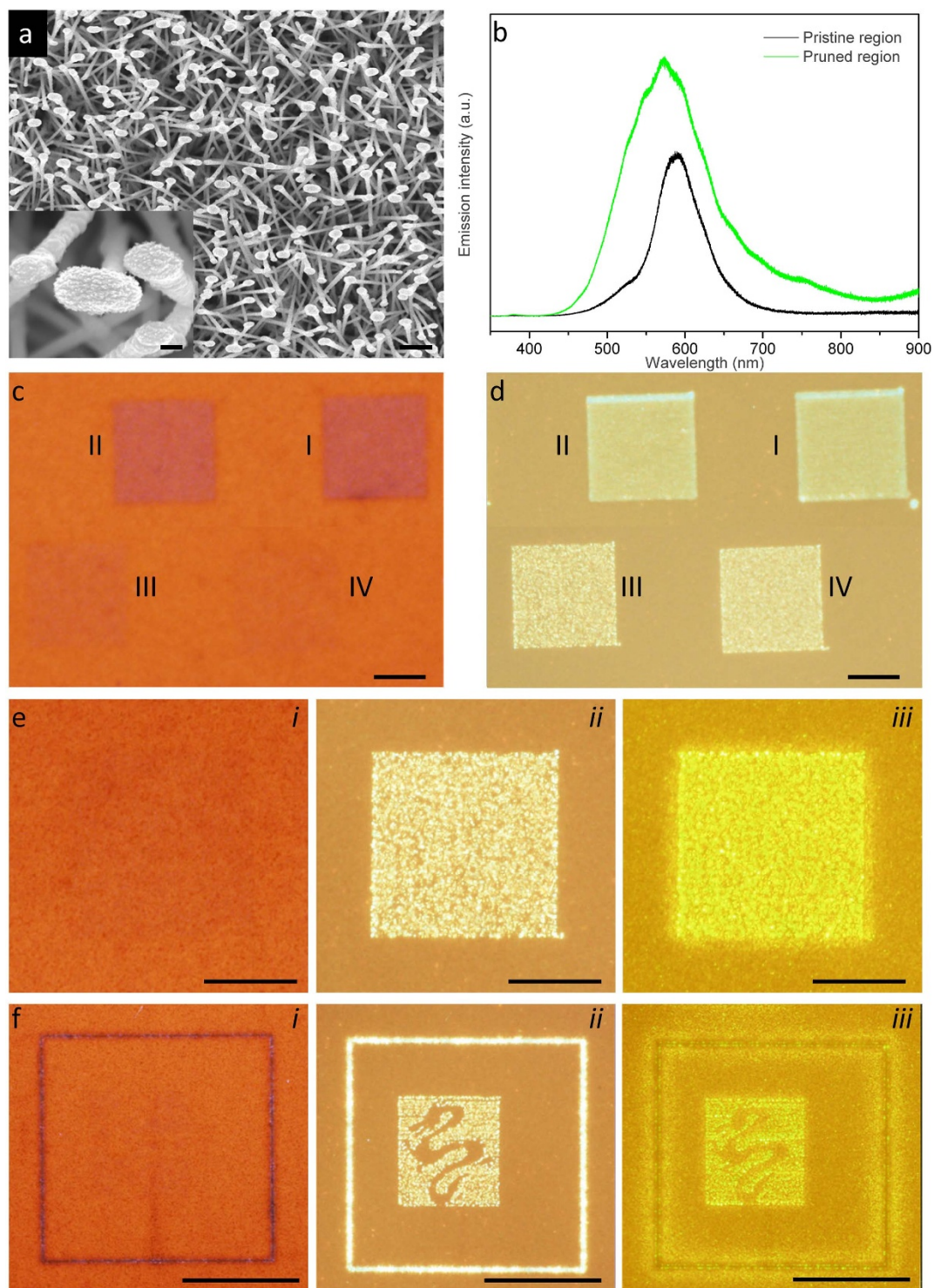


Figure 4 | (a) SEM image of the green laser pruned nanowires. Scale bar is 2 μm . Insert shows the high magnification image. Scale bar is 100 μm . (b) PL spectra for pristine (black curve) and laser pruned (green curve) regions. (c) Bright field optical and (d) FM images of created micro-squares. (e) and (f) Encryption application demonstration. (ei) Optical images of a square created on the sample, FM images of the square excited by (eii) UV light and (eiii) blue light. (fi) Optical images of a “dragon” created on the sample, FM images of the “dragon” excited by (fii) UV light and (fiii) blue light.

20. Meanwhile, D1 exhibits a rapid on/off switching behavior. Each photoresponse cycle consists of three distinct stages, a sharp rise, a steady state, and a sharp decay process to original state. The fast photocurrent rise and decay time is estimated from the photocurrent versus time plots and shown in Figure 5e. The rising response is determined to be as short as 28.5 ms which is even faster than the

recovery time of 35 ms. However, D2 shows more complex response processes to the photo illumination. Besides a rapid photoresponse process, both the rising and recovery processes comprised of a slowly varying components. The slow processes of rising and decaying time (Figure 5f) can be well fitted by the following exponential functions, respectively³⁶.

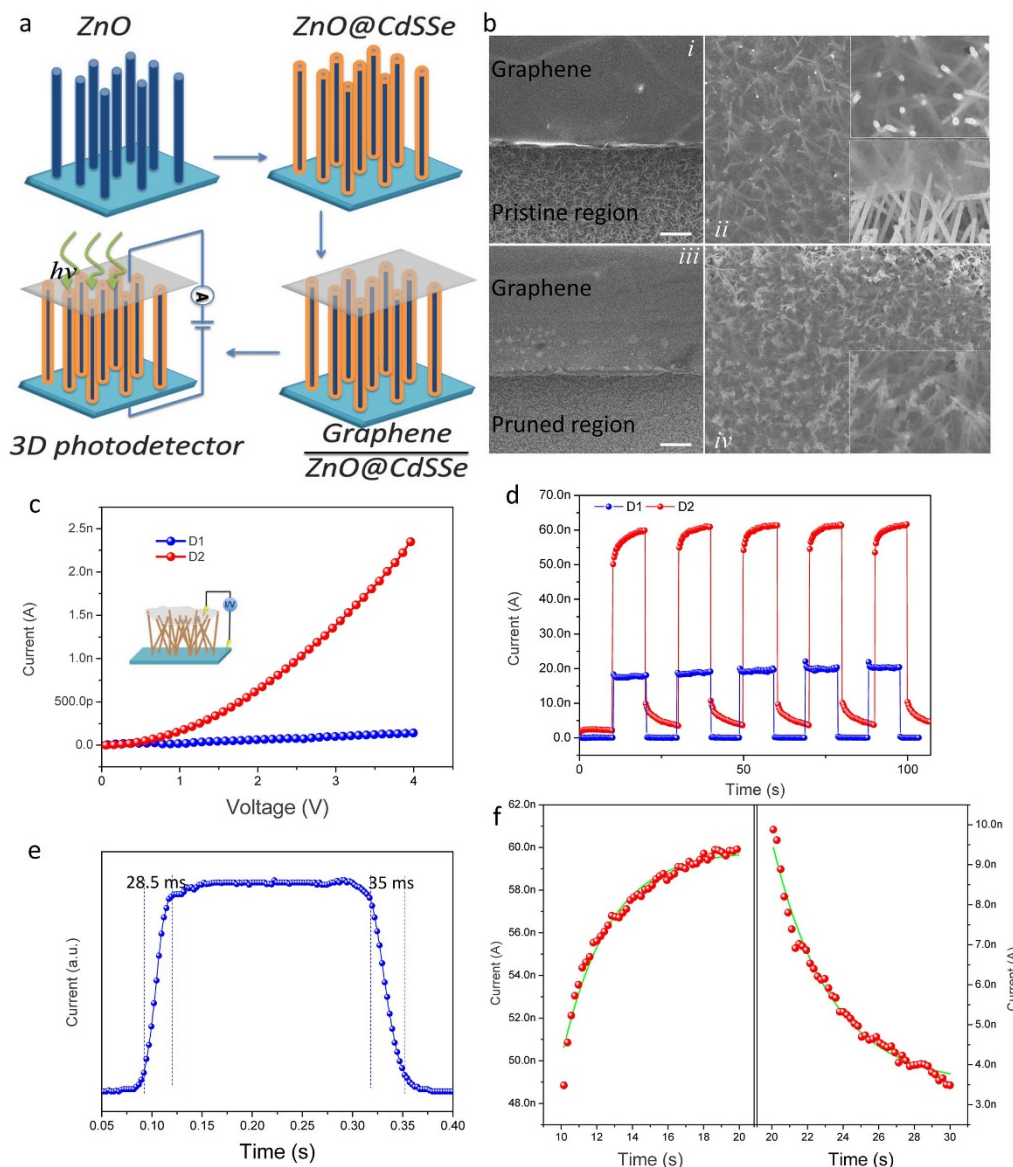


Figure 5 | (a) Diagram illustration of the 3D photodetector fabrication process. (b) SEM images of the hybrid structures. Scale bar is 10 μm . (c) Typical I-V characteristics of the devices. (d) Photoresponse characteristics of the devices. (e) Photoswitching rate test of D1. (f) Rising and decay time response analysis of the slow processes performed by D2.

$$I(t) = I_0 + A(1 - e^{-(t-t_0)/\tau}) \quad (2)$$

$$I(t) = I_0 + Ae^{-(t-t_0)/\tau} \quad (3)$$

where t_0 and t are the initial and final response time, I_0 is dark current, A is current amplitude, and τ is the characteristic time constant, related to the slow photoresponse processes observed. The slow rising and recovering response times of D2 obtained from curve fitting are ~ 2.6 s and ~ 3.3 s, respectively. We attribute such a slow photoresponse time to a heightened thermal effect of the induced defects by laser pruning. Generally, D2 exhibits higher photoresponsivity while D1 exhibits faster response time.

In summary, we have presented a high throughput and inherently efficient technique to directly modify type II core/shell heterostructures with multinary alloyed constituents, ZnO/CdSSe nanowire arrays. Well-defined micro structures are achievable via a simple focused laser beam. In addition, the fluorescence emission of the created micropatterns can be distinctly improved and precisely controlled with this effective technique. As a result, micro-steganography

at a selected location can be facilitated on the nanowire array surface. Moreover, the laser modified nanowire arrays exhibit more superior photoconductivity. This facilitates a high performance 3D photodetector constituted by the laser modified ZnO/CdSSe nanowire arrays as the main building block and monolayer graphene as the transparent top electrode.

Methods

ZnO nanowire arrays synthesis. ZnO nanowire arrays were synthesized via a chemical vapor deposition approach (CVD) in a sealed horizontal tube furnace³⁷. A 0.3 g powder mixture of ZnO and graphite in a molar ratio of 1 : 1 was placed in the bottom of a one-end-closed quartz tube. A piece of silicon wafer predeposited with a 200 nm ZnO seed layer by RF sputtering served as substrate and was inserted nearer to the open end. The quartz tube was placed into a large alumina work tube. The system was initially evacuated to a base pressure of 2.0×10^{-3} mbar before Ar gas mixed with 0.1% O_2 by volume of a total flow rate of 80 sccm was introduced. The pressure in the alumina work tube was raised to 2 mbar. The furnace was heated to 900°C and held at that temperature for 50 min. The growth temperature at the Si substrate was approximately 800°C.

ZnO/CdSSe core/shell nanowire arrays synthesis. To deposit the CdSSe outer-shells, the mixture of CdS and CdSe powder were placed into the reactor as the



precursor¹⁸. A piece of pre-prepared ZnO nanowire arrays was vertically inserted as the substrate. After the furnace was firstly evacuated to the base pressure, high-purity He gas was flown in the rate of 50 sccm. The system was ramped to 600°C and held for 10–30 min depending on the thickness of CdS/Se shell required. The local temperature at the substrate during the growth process was approximately 500°C. To avert the temperature influence for the chemical stoichiometry, a specially designed substrate holder was used to vertically fix the substrate to obtain CdS/Se shell with high-uniform stoichiometry. The composition of the shells was controlled by adjusting the molar ratio of CdS and CdSe powder. After that, the Si wafers covered with uniform colors (from yellow to dark-brown corresponding to the stoichiometry from CdS to CdSe) were obtained for further analysis.

Optical property measurement. The micro-PL spectra were carried out by the Renishaw inVia system with the excitation of a He-Cd laser centered at 325 nm. The time-resolved PL spectra were measured using a time-correlated single-photon counting system (PicoHarp300, PicoQuant). The samples were excited by a pulsed laser diode operating at 405 nm. The PL signal was dispersed by a monochromator (Acton, SpectroPro 2300i) and detected with a liquid-nitrogen-cooled charge-coupled device detector.

Transparent graphene electrode assembly. Monolayer graphene was synthesized on both sides of copper foils by the CVD method³⁵. A layer of PMMA resist was spin-coated onto one side of the copper foils. On the opposite side, the unprotected graphene was etched away with O₂ plasma by a RIE system. The exposed copper layer was etched using a solution of ammonium persulfate (7 gL⁻¹) and rinsed in deionized water. Finally, the resulting PMMA and graphene was transferred onto the desired hybrid nanowire arrays and acetone was utilized to remove the PMMA layer leaving behind a layer of graphene.

- Xu, J. *et al.* Arrays of ZnO/Zn_xCd_{1-x}Se Nanocables: Band Gap Engineering and Photovoltaic Applications. *Nano Lett.* **11**, 4138–4143 (2011).
- Smith, A. M. & Nie, S. Semiconductor Nanocrystals: Structure, Properties, and Band Gap Engineering. *Acc. Chem. Res.* **43**, 190–200 (2009).
- Regulacio, M. D. & Han, M.-Y. Composition-Tunable Alloyed Semiconductor Nanocrystals. *Acc. Chem. Res.* **43**, 621–630 (2010).
- Peng, X. Band Gap and Composition Engineering on a Nanocrystal (BCEN) in Solution. *Acc. Chem. Res.* **43**, 1387–1395 (2010).
- Ma, D. D. D., Lee, C. S., Au, F. C. K., Tong, S. Y. & Lee, S. T. Small-Diameter Silicon Nanowire Surfaces. *Science* **299**, 1874–1877 (2003).
- Gu, F. *et al.* Spatial Bandgap Engineering along Single Alloy Nanowires. *J. Am. Chem. Soc.* **133**, 2037–2039 (2011).
- Pan, A. *et al.* Color-Tunable Photoluminescence of Alloyed CdS_xSe_{1-x} Nanobelts. *J. Am. Chem. Soc.* **127**, 15692–15693 (2005).
- Swafford, L. A. *et al.* Homogeneously Alloyed CdS_xSe_{1-x} Nanocrystals: Synthesis, Characterization, and Composition/Size-Dependent Band Gap. *J. Am. Chem. Soc.* **128**, 12299–12306 (2006).
- Zhong, X., Feng, Y., Knoll, W. & Han, M. Alloyed Zn_xCd_{1-x}S Nanocrystals with Highly Narrow Luminescence Spectral Width. *J. Am. Chem. Soc.* **125**, 13559–13563 (2003).
- Ivanov, S. A. *et al.* Type-II Core/Shell CdS/ZnSe Nanocrystals: Synthesis, Electronic Structures, and Spectroscopic Properties. *J. Am. Chem. Soc.* **129**, 11708–11719 (2007).
- Lo, S. S., Mirkovic, T., Chuang, C.-H., Burda, C. & Scholes, G. D. Emergent Properties Resulting from Type-II Band Alignment in Semiconductor Nanoheterostructures. *Adv. Mater.* **23**, 180–197 (2011).
- Sung, T. K. *et al.* CdS/Se layer-sensitized TiO₂ nanowire arrays as efficient photoelectrodes. *J. Mater. Chem.* **21**, 4553–4561 (2011).
- Myung, Y. *et al.* Composition-Tuned ZnO–CdS/Se Core–Shell Nanowire Arrays. *ACS Nano* **4**, 3789–3800 (2010).
- Pan, A. L. *et al.* Si–CdS/Se Core/Shell Nanowires with Continuously Tunable Light Emission. *Nano Lett.* **8**, 3413–3417 (2008).
- Lim, S. X. *et al.* Directed Crystallization of CuSO₄·5H₂O onto Carbon Nanotube Microarchitectures. *J. Phys. Chem. C* **115**, 20964–20969 (2011).
- Teoh, H. F. *et al.* Microlandscaping on Graphene Oxide Film via Localized Decoration of Ag Nanoparticles. *Nanoscale* **6**, 3143–3149 (2013).
- Deng, S.-Z. *et al.* Thiol-Capped ZnO Nanowire/Nanotube Arrays with Tunable Magnetic Properties at Room Temperature. *ACS Nano* **4**, 495–505 (2009).
- Junpeng, L. *et al.* Facile One-Step Synthesis of CdS_xSe_{1-x} Nanobelts with Uniform and Controllable Stoichiometry. *J. Phys. Chem. C* **115**, 19538–19545 (2011).
- Chen, R. *et al.* Excitonic Properties and Near-Infrared Coherent Random Lasing in Vertically Aligned CdSe Nanowires. *Adv. Mater.* **23**, 1404–1408 (2011).

- Zhang, J., Zhang, X. & Zhang, J. Y. Size-Dependent Time-Resolved Photoluminescence of Colloidal CdSe Nanocrystals. *J. Phys. Chem. C* **113**, 9512–9515 (2009).
- Liu, H. W. *et al.* Temperature and composition dependence of photoluminescence dynamics in CdS_xSe_{1-x} (0 ≤ x ≤ 1) nanobelts. *J. Appl. Phys.* **111**, 073112–073116 (2012).
- Xu, X. *et al.* Dynamics of Bound Exciton Complexes in CdS Nanobelts. *ACS Nano* **5**, 3660–3669 (2011).
- Zhao, H. & Kalt, H. Energy-dependent Huang-Rhys factor of free excitons. *Phys. Rev. B* **68**, 125309 (2003).
- Feldmann, J. *et al.* Linewidth dependence of radiative exciton lifetimes in quantum wells. *Phys. Rev. Lett.* **59**, 2337–2340 (1987).
- Karaickaj, D., Mascarenhas, A., Choi, J. H., Graff, R. & Strano, M. S. Temperature behavior of the photoluminescence decay of semiconducting carbon nanotubes: The effective lifetime. *Phys. Rev. B* **75**, 113409 (2007).
- Lu, J. *et al.* Transient Photoconductivity of Ternary CdS/Se Nanobelts As Measured by Time-Resolved Terahertz Spectroscopy. *J. Phys. Chem. C* **117**, 12379–12384 (2013).
- Liu, H. *et al.* Defect Engineering in CdS_xSe_{1-x} Nanobelts: An Insight into Carrier Relaxation Dynamics via Optical Pump–Terahertz Probe Spectroscopy. *J. Phys. Chem. C* **116**, 26036–26042 (2012).
- Lu, J., Lim, X., Zheng, M., Mhaisalkar, S. G. & Sow, C.-H. Direct Laser Pruning of CdS_xSe_{1-x} Nanobelts en Route to a Multicolored Pattern with Controlled Functionalities. *ACS Nano* **6**, 8298–8307 (2012).
- Bae, S. *et al.* Roll-to-roll production of 30-inch graphene films for transparent electrodes. *Nat Nano* **5**, 574–578 (2010).
- Wang, X., Zhi, L. & Mullen, K. Transparent, Conductive Graphene Electrodes for Dye-Sensitized Solar Cells. *Nano Lett.* **8**, 323–327 (2007).
- Tung, V. C. *et al.* Low-Temperature Solution Processing of Graphene–Carbon Nanotube Hybrid Materials for High-Performance Transparent Conductors. *Nano Lett.* **9**, 1949–1955 (2009).
- Suk, J. W. *et al.* Transfer of CVD-Grown Monolayer Graphene onto Arbitrary Substrates. *ACS Nano* **5**, 6916–6924 (2011).
- Lim, S. *et al.* Assembly of suspended graphene on carbon nanotube scaffolds with improved functionalities. *Nano Res.* **5**, 783–795 (2012).
- Hamilton, M. C., Martin, S. & Kanicki, J. Thin-film organic polymer phototransistors. *Electron Devices, IEEE Transactions on* **51**, 877–885 (2004).
- Tang, Q. *et al.* Photoswitches and Phototransistors from Organic Single-Crystalline Sub-micro/nanometer Ribbons. *Adv. Mater.* **19**, 2624–2628 (2007).
- Bera, A. & Basak, D. Carrier relaxation through two-electron process during photoconduction in highly UV sensitive quasi-one-dimensional ZnO nanowires. *Appl. Phys. Lett.* **93**, 053102 (2008).
- Li, X. *et al.* Large-Area Synthesis of High-Quality and Uniform Graphene Films on Copper Foils. *Science* **324**, 1312–1314 (2009).

Acknowledgments

Lu JP and Sow CH gratefully acknowledge the financial support from Singapore National Research Foundation under CRP Award No. NRF-CRP-4-2008-03.

Author contributions

J.L. and H.L. performed experiments and analyzed the data. J.L. and H.L. wrote the manuscript. C.H.S. gave scientific advice. E.S.T. and C.H.S. commented on the manuscript. M.Z., H.Z. and S.X.L. gave scientific suggestions. All authors contributed to discussion and reviewed the manuscript.

Additional information

Supplementary information accompanies this paper at <http://www.nature.com/scientificreports>

Competing financial interests: The authors declare no competing financial interests.

How to cite this article: Lu, J. *et al.* Laser Modified ZnO/CdS/Se Core-Shell Nanowire Arrays for Micro-Steganography and Improved Photoconduction. *Sci. Rep.* **4**, 6350; DOI:10.1038/srep06350 (2014).



This work is licensed under a Creative Commons Attribution-NonCommercial-NoDerivs 4.0 International License. The images or other third party material in this article are included in the article's Creative Commons license, unless indicated otherwise in the credit line; if the material is not included under the Creative Commons license, users will need to obtain permission from the license holder in order to reproduce the material. To view a copy of this license, visit <http://creativecommons.org/licenses/by-nc-nd/4.0/>